Spray Coating Experiments: Setups and Methodologies

The latest eBook from Advanced Optical Metrology. Download for free.

Spray Coating Experiments: Setups and Methodologies, is the third in our Thin Films eBook series. This publication provides an introduction to spray coating, three article digests from Wiley Online Library and the latest news about Evident's Image of the Year Award 2022.

Wiley in collaboration with Evident, are committed to bridging the gap between fundamental research and industrial applications in the field of optical metrology. We strive to do this by collecting and organizing existing information, making it more accessible and useful for researchers and practitioners alike.

EVIDENT
OLYMPUS

WILEY

NANO · MICRO small
www.small-journal.com

Phase-Modulated Multidimensional Perovskites for High-Sensitivity Self-Powered UV Photodetectors

Xinyu Zhang, Ziqing Li, Tingting Yan, Li Su, and Xiaosheng Fang**

2D Ruddlesden-Popper perovskites (PVKs) have recently shown overwhelming potential in various optoelectronic devices on account of enhanced stability to their 3D counterparts. So far, regulating the phase distribution and orientation of 2D perovskite thin films remains challenging to achieve efficient charge transport. This work elucidates the balance struck between sufficient gradient sedimentation of perovskite colloids and less formation of small-*n* phases, which results in the layered alignment of phase compositions and thus in enhanced photoresponse. The solvent engineering strategy, together with the introduction of poly(3,4-ethylenedioxythiophene):polystyrene sulfonate (PEDOT:PSS) and $PC_{71}BM$ layer jointly contribute to outstanding self-powered performance of indium tin oxide/PEDOT:PSS/PVK/$PC_{71}BM$/Ag device, with a photocurrent of 18.4 µA and an on/off ratio up to 2800. The as-fabricated photodetector exhibits high sensitivity characteristics with the peak responsivity of 0.22 A W^{-1} and the detectivity up to 1.3×10^{12} Jones detected at UV-A region, outperforming most reported perovskite-based UV photodetectors and maintaining high stability over a wide spectrum ranging from UV to visible region. This discovery supplies deep insights into the control of ordered phases and crystallinity in quasi-2D perovskite films for high-performance optoelectronic devices.

1. Introduction

In recent years, 3D organic–inorganic hybrid perovskite (OHP) materials have drawn much attention in the field of photodetection, owing to outstanding optoelectronic properties, such as high optical absorption coefficient, high carrier mobility, long carrier diffusion length as well as low-temperature production capacity and solution processability. These superior optoelectronic performances benefit from the advantages of organic and inorganic semiconductors together with the crystal structure properties of halide perovskite (PVK).[1–3] However, due to the presence of volatile small-volume organic cations and surface defects, the crystal structure of 3D OHP materials is susceptible to damage under the effect of moisture, oxygen, heat, and UV light.[4,5] Besides, ion migration triggered by soft lattices and degradation intermediates will also affect their stability.[2,4] Chemically accomplished dimensional reduction is proved a brilliant strategy to alleviate the above-mentioned issues, the most representative of which is 2D Ruddlesden-Popper (RP) perovskite materials with the structural formula $R_2A_{n-1}B_nX_{3n+1}$ ($n = 1$), where R refers to a massive organic cation acting as a spacer to "cut" the 3D perovskite into atomically thick metal halide layers along a specific crystallographic orientation, while n denotes the number of inorganic octahedral $[BX_6]^{4-}$ sheet layers sandwiched between two organic layers.[1,6] The adjacent organic and inorganic layers are stacked together under weak van der Waals forces and hydrophobic forces, which leads to the increase of formation energy and thus imparts higher stability to the perovskite materials.[6,7] Nevertheless, the strong insulating nature of the organic layers results in the formation of the multiquantum-well electronic structure in 2D RP perovskite, where bulk organic cations serve as dielectric barriers and strongly confine the electron–hole pairs (excitons) in 2D space.[1,8] The strong quantum confinement, dielectric shielding, and multiexciton resonance in the 2D RP perovskite will jointly inhibit the charge transport between adjacent layers and induce the transformation of excitonic properties including increased exciton binding energy, wider bandgap and decreased carrier mobility, which cause an unfavorable impact on the optoelectronic properties of perovskite materials.[9,10]

To address the above issues, various optimization strategies have been proposed to modulate the composition of perovskite materials. Smith et al. achieved layered perovskites with specific n values by tuning the stoichiometric ratio of the precursor solution composition so that the short-chain organic groups in 3D OHPs were partially replaced by bulky insulating organic groups, thus striking a balance between the strong stability of pure 2D RP perovskites R_2BX_4 and the excellent charge transport properties of 3D OHPs ($n = \infty$).[9,11] In other words, the

X. Zhang, T. Yan, L. Su, X. Fang
Department of Materials Science
State Key Laboratory of Molecular Engineering of Polymers
Fudan University
Shanghai 200433, P. R. China
E-mail: xshfang@fudan.edu.cn
Z. Li, X. Fang
Shanghai Frontiers Science Research Base of Intelligent Optoelectronics and Perception
Institute of Optoelectronics
Fudan University
Shanghai 200433, P. R. China
E-mail: lzq@fudan.edu.cn
The ORCID identification number(s) for the author(s) of this article can be found under https://doi.org/10.1002/smll.202206310.

DOI: 10.1002/smll.202206310

modulation of excitonic properties is realized by increasing the quantum well thickness (n) whereby the quantum and dielectric confinement effects within 2D perovskites are minimized and the exciton–photon coupling is suppressed.[12,13] These 2D/3D hybrid perovskite materials are also known as quasi-2D perovskites, and their photodetectors are found to possess better optoelectronic properties as the value of n increases, including photocurrent, responsivity, on/off ratio and response time.[12,14] Moreover, the bulky organic cations in quasi-2D perovskites can constrain the formation of crystal defects, and this passivation effect can endow the photodetectors with higher detectivity.[12]

In addition to the composition modulation, the optimization of crystallographic orientation within quasi-2D perovskite films also contributes to the improvement of the optoelectronic performance. The lateral structure with simple fabrication processes has been adopted for most of the early reported perovskite photodetectors, whereas the wide electrode spacing (>5 µm) of lateral structure devices poses an obstacle to efficient charge transport.[6,15] In contrast, the ultrashort electrode spacing of the vertically structured device, where the 2D $[A_{n-1}B_nX_{3n+1}]^{2-}$ layers oriented perpendicular to the substrate, enables high gain and high optical response at low operating voltage (or zero bias).[16] Considering the "sliding" effect of the insulating organic cations, quasi-2D perovskite materials exhibit distinct charge transport anisotropy, with intralayer transport far better than interlayer transport.[12] Tsai et al. took the lead in preparing quasi-2D perovskite materials with vertical crystallographic orientation by using hot-casting method, and demonstrated the remarkable effect of orientation regulation on improving charge transport through multiple tests.[17] On this basis, intermittent spin-coating, thermal-pressed effect and other strategies have been successively reported to finely regulate the oriented growth of quasi-2D perovskites, and the resulting photodetector exhibits high responsivity of ≈0.25 A W^{-1} and high specific detectivity of $\approx 10^{12}$ Jones at zero bias.[18,19] On the downside, the above strategies are poorly reproducible and have strict demands on equipment and process conditions. In comparison, it is more feasible to preregulate the perovskite precursor solution, such as solvent engineering and additive induction.[20,21]

Furthermore, it is worth noting that quasi-2D perovskites prepared by traditional solution methods are not always pure-phase products, and the phase distribution greatly affects the final optoelectronic performance.[12] Due to the competitive growth of heterogeneous films triggered by the heat transfer during the hot-casting or thermal annealing process, the final products are often mixed-phase films composed of random stacking of perovskite layers with different n values, and the energy- or charge-transfer characteristics resulted from this special structure will greatly influence the optoelectronic performance.[12,22] Therefore, the phase distribution of quasi-2D perovskites should also be brought to the forefront. By adopting various approaches such as process temperature control, solvent engineering and ligand exchange, quasi-2D perovskites with continuous phase distribution can be obtained, and the high-gain self-powered photodetectors can be fabricated afterward.[23–25]

Herein, quasi-2D perovskites denoted as $PEA_2MA_3Pb_4I_{13}$ ($PEA^+ = C_6H_5(CH_2)_2NH_3^+$, $MA^+ = CH_3NH_3^+$) are prepared through hot-casting and solvent-engineering strategies. The modulation of dimethyl sulfoxide (DMSO) content in the *N*,*N*-dimethylformamide (DMF) solution is shown to significantly improve the phase distribution along the vertical direction of perovskite films, which promotes the efficient separation of photogenerated carriers under the effect of well-arranged cascaded energy band alignment, thereby leading to enhanced optoelectronic performance. Moreover, defects in perovskite films are greatly passivated due to the introduction of poly(3,4-ethylene-dioxythiophene):polystyrene sulfonate (PEDOT:PSS) layer, along with the enhancement of vertical orientation, which facilitates the charge transport. In consequence, the as-fabricated indium tin oxide (ITO)/PEDOT:PSS/PVK/$PC_{71}BM$/Ag device achieves high sensitivity to a broad spectrum of light without external bias voltage. This work provides new insights into the phase distribution and orientation regulation based on gradient 2D/3D perovskite thin films for desired high-performance photodetectors.

2. Results and Discussion

The high-resolution X-ray photoelectron spectra (XPS) of as-fabricated quasi-2D perovskite films are shown in Figure S1 in the Supporting Information, where all peaks can be assigned to main constituent elements of $PEA_2MA_3Pb_4I_{13}$. **Figure 1**a exhibits the X-ray diffraction (XRD) patterns of the $PEA_2MA_3Pb_4I_{13}$ films with different concentrations of DMSO, where two prominent diffraction peaks correlated with (111) and (202) crystallographic planes can be observed at the identical peak positions of 14.03° and 28.35°,[18] respectively, indicating the preferred orientation within quasi-2D RP perovskite films along the vertical direction under the influence of DMSO, which is consistent with previous reports.[26] Note that the diffraction intensity ratio $I_{(202)}/I_{(111)}$ keeps ascending with the increase of DMSO content (see Figure S2 and Table S1, Supporting Information), implying an uprising degree of vertical orientation.[27] While on the other hand, the variation of DMSO content leads to perceptible changes of the diffraction intensity and the full width at half-maximum (FWHM) of the two dominant diffraction peaks, as demonstrated in Figure S3 in the Supporting Information. When the DMSO content reaches 10%, both (111) and (202) diffraction peaks possess the maximum diffraction intensity and the minimum FWHM value, suggesting the optimized crystallinity as well as the enlarged crystallite size of the perovskite films, according to the Scherrer equation,[28] which can also be found in the corresponding field-emission scanning electron microscopy (FESEM) images (Figure 1b). The high quality growth of perovskite films can be attributed to the synergistic effect of fast nucleation and slow crystallization behavior, as for the former, the hot-casting technique promptly induce the supersaturation of precursor solution for instant formation of nuclei, while the crystallization rate can be significantly retarded via solvent engineering with DMSO, as depicted in Figure S4 in the Supporting Information. Due to the relatively high solvent polarity, DMSO will exhibit a high affinity for metal halides and will form stronger hydrogen bonds with organic cations in the presence of $S^{\delta+} = O^{\delta-}$ polarized bond, thus acting as a crystallization retardant through forming intermediate solvated phase.[29]

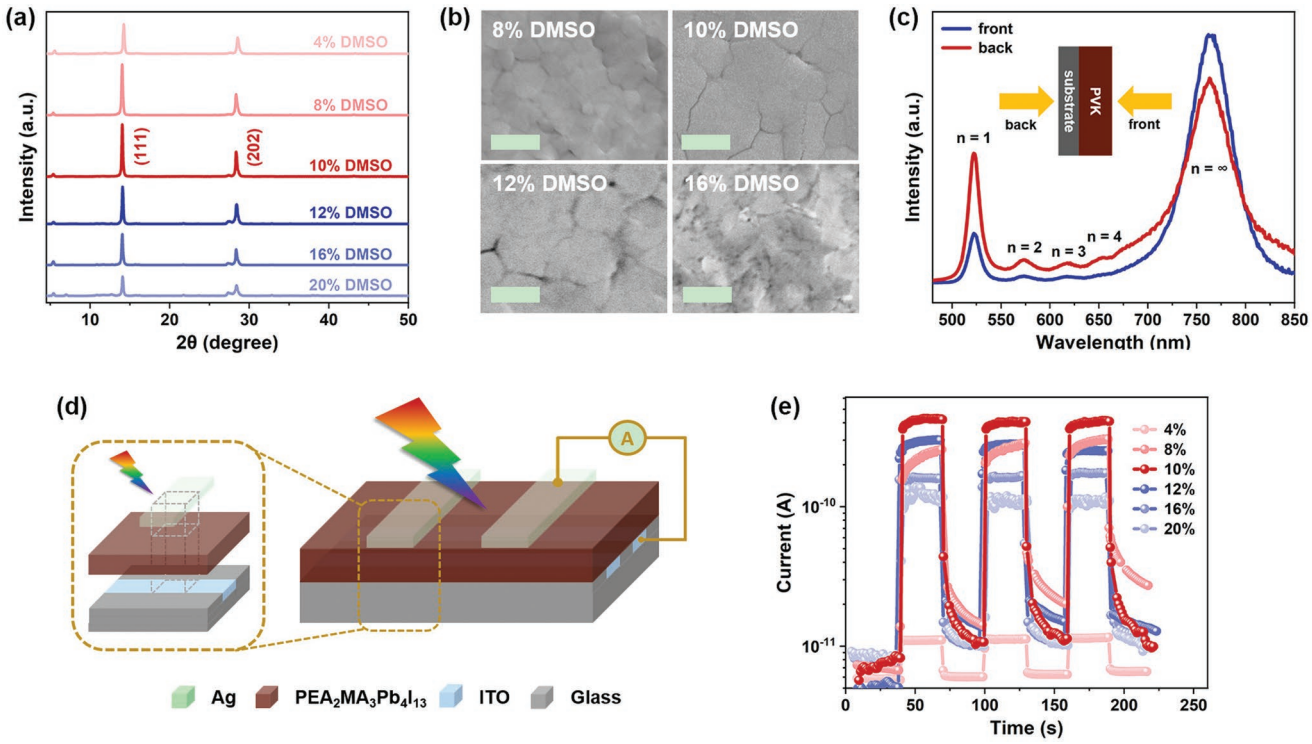

Figure 1. a) XRD patterns and b) Top-view FESEM images of $PEA_2MA_3Pb_4I_{13}$ films prepared at different Dimethyl sulfoxide contents (scale bar: 1 µm). c) Steady-state PL spectra of the $PEA_2MA_3Pb_4I_{13}$ films illuminated from the perovskite film side and the glass side. d) Schematic illustration of the ITO/PVK/Ag photodetector. e) The semi-logarithmic *I–t* curves of ITO/PVK/Ag photodetectors prepared at different DSMO contents, measured under 400 nm illumination without external bias voltage.

Figure 1c shows the steady-state photoluminescence (PL) spectra of the $PEA_2MA_3Pb_4I_{13}$ films prepared with 10% DMSO precursor, excited from both sides of the sample under 465 nm illumination with the same optical power, where the emission peaks at the wavelength of 522, 574, 620, 654, and 763 nm can be ascribed to the n = 1, 2, 3, 4, and ∞ phases, respectively. As the penetration depth of the excitation light is notably less than the thickness of perovskite layer, the PL spectra irradiated from the front and back side give a rather realistic picture of the phase distribution at the top and bottom of the perovskite film, where the effect of substrate is negligible since the ITO glass has an average light transmission rate of over 90% under 400–900 nm illumination. Note that the appearance of small-n emission peaks in frontal PL spectrum can be ascribed to the carrier migration from 3D to 2D (quasi-2D) phases and vice versa, where the excitation energy is more inclined to transfer to large-n phases considering the narrower bandgap, leading to dominant $n = \infty$ emission peak even in the back-side PL spectrum.[30,31] When excited from the back side of the perovskite films, the PL intensity in the spectrum range corresponding to the small-n phases increases compared to that of the frontal excitation, together with the intensity loss at the emission band of $n = \infty$ composition, thus proving the bottom-up self-assembled phase alignment in the perovskite films with a comparatively gradient sequence of n values from low to high. This vertical distribution characteristic can be explained by the sedimentation equilibrium on account of the colloidal feature of the perovskite precursors and the intrinsic volume difference between phenethylammonium iodide (PEAI)-PbI_2 and methylammonium iodide (MAI)-PbI_2 clusters.[32]

To evaluate the optoelectronic performance of the above perovskite films, a series of devices with the vertical structure of ITO/PVK/Ag are constructed, as illustrated in Figure 1d. Figure 1e shows the semi-logarithmic current–time (*I–t*) curves measured under 400 nm illumination without external bias voltage, where stable on/off switching cycles can be observed at different DMSO contents, indicating the repeatable photoresponse of the ITO/PVK/Ag photodetector. With the alteration of DMSO content, the dark current tends to stay constant, whereas the photocurrent varies significantly and achieves the maximum at 10% DMSO content with an on/off ratio of 65. This could be clearly attributed to its uniform morphology, high crystallinity and large crystallite size, namely the reduction of grain boundaries which leads to the sharp decline in trap-state density along with the restraint of nonradiative carrier combination, facilitating the rapid charge transport and thus endowing the optoelectronic devices with faster photoresponse. Beyond that, the phase distribution pattern in these films plays a decisive role in the improvement of optoelectronic performance, especially when high-quality crystallization is guaranteed, thereby UV–vis absorption spectroscopy was performed for further investigation. As shown in **Figure 2**a–c, the curve trends including dominant peak positions of the UV–vis absorption spectra are in exact accordance with those of PL spectra, verifying the layered alignment of phase compositions along the perpendicular direction. While it is worth noting that the front

and back absorption of the same sample exhibit increasingly pronounced variance as the DMSO content rises from 8% to 12%, especially at the wavelength assigned to small-*n* phases. This is due to the suppression of solvent evaporation rate as the DMSO content increases, which provides sufficient time for colloidal clusters to achieve gradient sedimentation while minimally affected by the updraft of evaporating solvent, thus promoting the segregation of small-*n* and large-*n* phases in the vertical direction and consequently forming a more explicit gradient arrangement, as depicted in Figure 2d. In this regard, the regulation of annealing temperature of perovskite films can also be considered as a means of controlling the solvent evaporation rate. As demonstrated in Figure 2e, the evaporation rate of solvent can be effectively retarded by reducing the annealing temperature within a certain range, which ultimately contributes to optimized crystalline quality and phase distribution for better optoelectronic performance.

Since the optical bandgap (E_g) increases with reduced dimensionality under the impact of quantum and dielectric confinement,[33] the regulated phase distribution in the films will induce the formation of expected cascaded type-II energy band arrangement perpendicular to the substrate, which brings about spontaneous separation of photogenerated carriers. Figure 2f displays the band structure of layered perovskites illustrated according to E_g values derived from the Tauc plot (Figure 2g), where the built-in electric field is constructed from small-*n* phases to large-*n* phases on account of the intrinsic gradient energy levels. When exposed to incident light, the electron–hole pairs generated in layered perovskites will separate rapidly under the driving force of built-in electric field, followed by electron drift toward the top electrode and hole migration toward the bottom electrode, resulting in a photocurrent without applying any external bias. It should be pointed out that excluding the factor of deteriorating crystalline quality, the degradation of photoresponse performance triggered by excessive DMSO content may also arise from the unfavorable phase distribution with massive small-*n* phases. Specifically, in the presence of ever-rising DMSO content, additional energy is required to break the hydrogen bonds between DMSO and organic cations, leading to a lack of energy for the self-assembly of large-*n* perovskites, while the formation of thermodynamically favorable small-*n* phases is preferred.[29] Under the effect of sufficient sedimentation equilibrium, more small-*n* phases accumulate at the bottom of the film, as confirmed by the intensity growth of the $n = 1$ absorption band from the backside test, and these phases tend to act as trap states for carrier recombination,[34] which would eventually pose an obstacle to excellent optoelectronic performance.

To maximize the self-powered performance of $PEA_2MA_3Pb_4I_{13}$ integrated photodetectors, the vertical photodetectors were designed based on the perovskite films prepared with precursor solution containing 10% DMSO, along with the introduction of PEDOT:PSS layer and [6,6]-phenyl-C_{71}-butyric acid methyl ester ($PC_{71}BM$) layer, as schematically shown in **Figure 3**a. The cross-sectional FESEM image of PEDOT:PSS/PVK/$PC_{71}BM$/Ag layered structure is presented in Figure 3b, where the perpendicular column-like crystalline grains are observed in the as-fabricated perovskite films, with good continuity, surface coverage, and a proper layer thickness of around 280 nm for well-balanced light absorption and charge transport.[35] The perovskite photodetectors with the configuration of ITO/PEDOT:PSS/PVK/Ag, ITO/PVK/$PC_{71}BM$/Ag, and ITO/PEDOT:PSS/PVK/$PC_{71}BM$/Ag exhibit enhanced photoelectric response capability in comparison with the ITO/PVK/Ag device, with a remarkable increase in both the dark current and the photocurrent (Figure 3c), demonstrating the role of intermediate layers in facilitating carrier extraction and transport as well as in the modification of interfacial contact. Under 400 nm illumination without external bias voltage, the ITO/PEDOT:PSS/PVK/$PC_{71}BM$/Ag device achieves outstanding self-powered performance with a photocurrent of 1.84×10^{-5} A and an on/off ratio up to 2800, which are remarkably higher than those of other $PEA_2MA_3Pb_4I_{13}$ integrated devices in this work. As expected, *I*–*V* curve in the dark condition shows obvious rectifying behavior (Figure 3d), which results from the combined effect of gradient phase distribution of the perovskite films, Schottky contacts, and the *p*-*i*-*n* type heterojunction consisting of PEDOT:PSS, $PEA_2MA_3Pb_4I_{13}$ and $PC_{71}BM$ layer. Figure 3e reveals a wide spectrum response ranging from UV to visible region, which can be assigned to interlaced optical bandgaps. To quantify the photodetection capability of photodetectors, the responsivity (R_λ) is introduced to evaluate the response efficiency to the optical signal, given by[36]

$$R_\lambda = \frac{I_{ph} - I_{dark}}{P_\lambda S} \tag{1}$$

where I_{ph} is the photocurrent, I_{dark} is the dark current, P_λ is the light power density at a particular wavelength (λ), and S is the effective illumination area of the photodetector. The responsivity of the ITO/PEDOT:PSS/PVK/$PC_{71}BM$/Ag device is then depicted in Figure 3f (blue dotted line) as a function of wavelength, where the maximum responsivity of 0.22 A W^{-1} is possessed at 330 nm, and the tested photodetector consistently maintains a responsivity greater than 0.12 A W^{-1} up to 600 nm. Figure S5a in the Supporting Information compared the responsivity curves of photodetectors prepared under different DMSO content conditions, verifying the improved phase distribution in perovskite films after solvent engineering, which leads to better assembly of vertical heterojunctions, thus drastically expediting the spatial separation of photogenerated electrons and holes. Notably, the apparent discrepancy in responsivity curves, especially ranging from 460 to 600 nm, can be corresponded to the superior alignment of small-*n* phases. As demonstrated in Figure 3g and Table S2 in the Supporting Information, the as-fabricated self-powered device in this work shows better photoresponse performance in the UV region than other OHP-based photodetectors reported in the previous studies.

The detectivity (D^*) and external quantum efficiency (EQE) are further calculated to access the capacity for detecting weak light signals and the photoelectric conversion efficiency of the device, respectively, according to the following equations[37]

$$D^* = \frac{R_\lambda \sqrt{S}}{\sqrt{2eI_{dark}}} \tag{2}$$

$$EQE = \frac{hc}{e}\frac{R_\lambda}{\lambda} \tag{3}$$

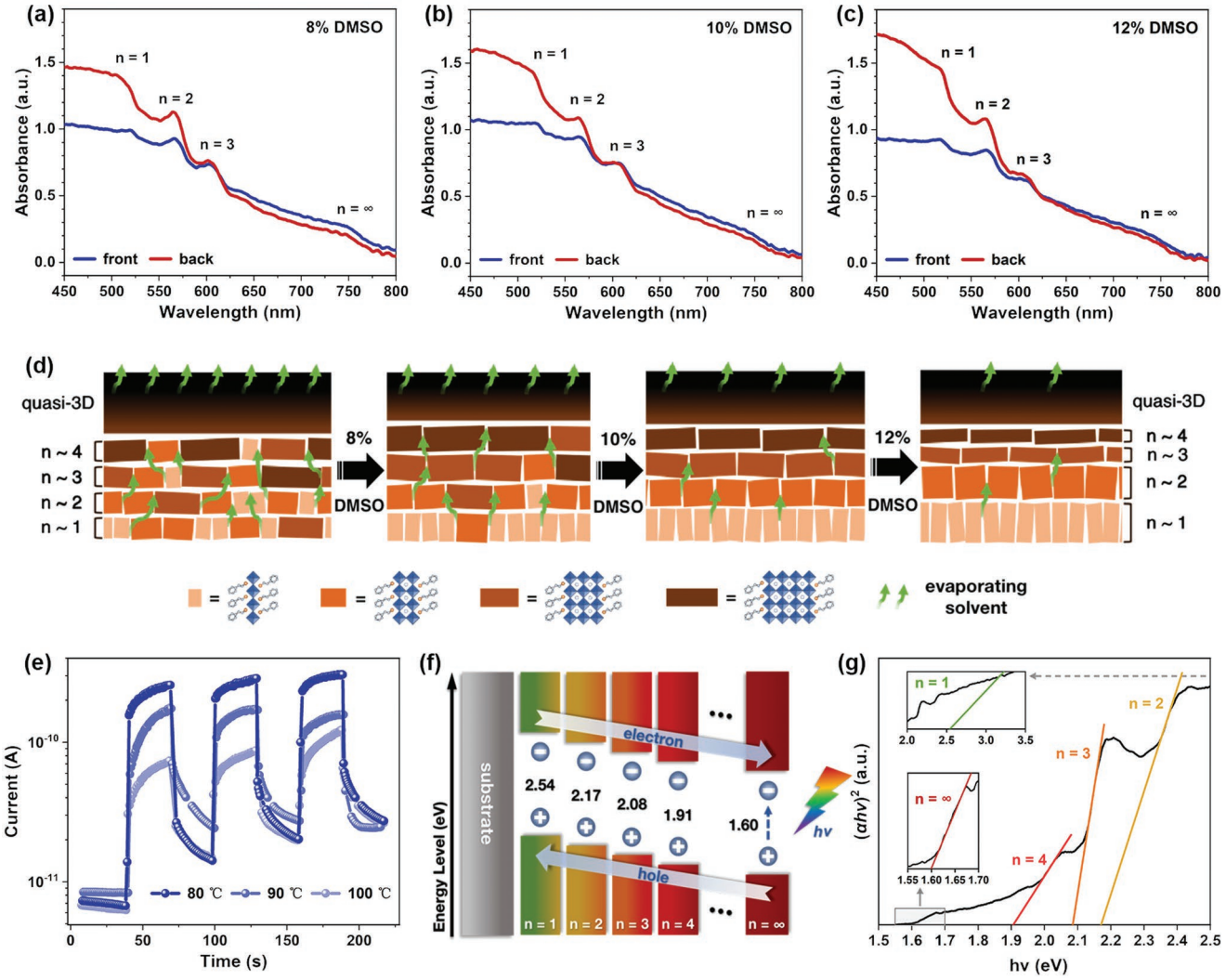

Figure 2. UV–vis absorption spectra of $PEA_2MA_3Pb_4I_{13}$ films prepared at a) 8%, b) 10%, and c) 12% DMSO content, illuminated from the perovskite film side and the glass side. d) Schematic illustration of the phase arrangement process under different DMSO content conditions. e) Schematic illustration of the band alignment in layered perovskite films. f) Tauc plots of $PEA_2MA_3Pb_4I_{13}$ films. The linear extrapolation is used to determine the optical bandgap E_g. The insets are local enlarged curves. g) The semi-logarithmic *I–t* curves of ITO/PVK/Ag photodetectors prepared at different annealing temperatures, measured under 400 nm illumination without external bias voltage.

where *e*, *h*, and *c* respectively denote the elementary electron charge, Planck's constant, and the light viscosity. As shown in Figure 3f, the variation tendency of detectivity with wavelength shares striking similarity with that of responsivity. The detectivity reaches a maximum value of 1.3×10^{12} Jones at 330 nm and then stays greater than 6.7×10^{11} Jones in the long wavelength region. Likewise, Figure S5b in the Supporting Information demonstrates boosted detectivity of the photodetector fabricated with 10% DMSO precursor compared with others, indicating the overall enhancement of photodetection performance by adjusting DMSO content. The *EQE* keeps over 30% within the wavelength range of 280–600 nm and achieves its peak value of 83% at 330 nm (Figure S5c, Supporting Information).

As plotted in Figure 3h, under 400 nm illumination without external bias voltage, the photocurrent value of as-fabricated device increases obviously with the light power density, owing to the proportional relationship between the number of photogenerated carriers and absorbed photon flux.[38] The dependence of the photocurrent on light power density obeys the power equation given by

$$I_{ph} = \alpha P^{\beta} \tag{4}$$

where α represents a constant related to specific wavelength and the exponential value β determines the response of photocurrent to the light power density. Generally, the value of β is between 0 and 1 as a result of complex process of electron–hole generation, trapping, transfer, and recombination within the device. The fitted curve based on the aforementioned equation in Figure 3h presents a linear behavior of $\beta = 0.93$, where β is extremely close to 1, implying suppressed recombination loss of electrons and holes which eventually favors the increase of photocurrent.

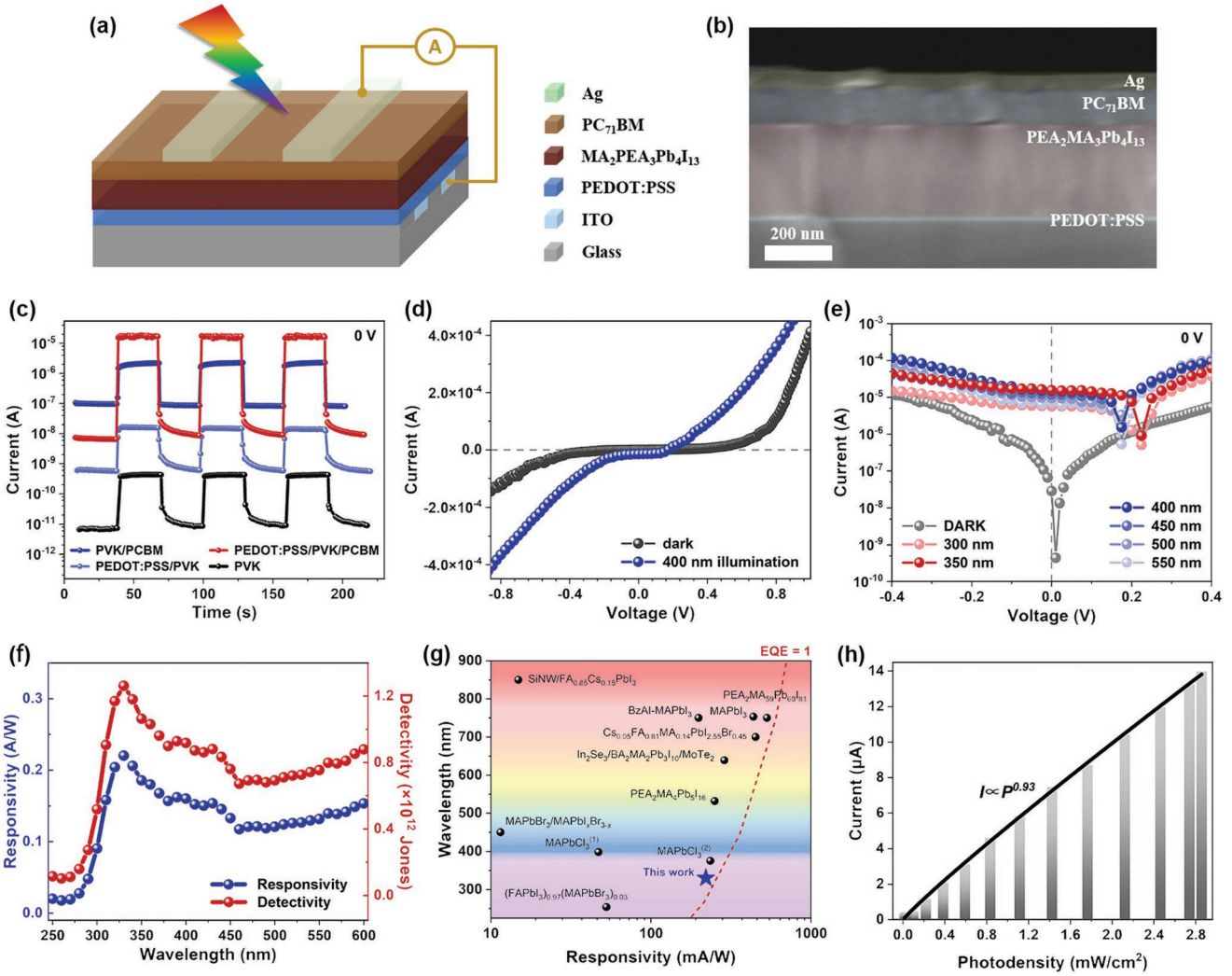

Figure 3. a) Schematic illustration of the ITO/PEDOT:PSS/PVK/$PC_{71}BM$/Ag photodetector. b) Cross-sectional FESEM image of the PEDOT:PSS/PVK/$PC_{71}BM$/Ag layered structure spin-coated on the Si substrate. c) The semi-logarithmic *I–t* curves of ITO/PVK/Ag, ITO/PEDOT:PSS/PVK/Ag, ITO/PVK/$PC_{71}BM$/Ag, and ITO/PEDOT:PSS/PVK/$PC_{71}BM$/Ag photodetectors. d) The linear *I–V* curves and e) semi-logarithmic *I–V* curves of the ITO/PEDOT:PSS/PVK/$PC_{71}BM$/Ag photodetector under the dark condition and UV illumination. f) The responsivity curve and the detectivity curve as a function of wavelength for ITO/PEDOT:PSS/PVK/$PC_{71}BM$/Ag photodetector. g) Wavelength and responsivity of the ITO/PEDOT:PSS/PVK/$PC_{71}BM$/Ag photodetector and reported photodetectors in the previous studies. The reference data are from Table S1 in the Supporting Information. h) Photocurrent as a function of light power density for ITO/PEDOT:PSS/PVK/$PC_{71}BM$/Ag photodetector.

To further analyze the effect of employing PEDOT:PSS layer in promoting orientational growth and desired phase distribution of perovskite films, a series of characterizations were adopted, the results of which are shown in **Figure 4**. Compared to pristine $PEA_2MA_3Pb_4I_{13}$, the perovskite films grown on PEDOT:PSS layer possess a smoother XRD pattern (Figure 4a), with the vanishing of diffraction peaks (marked as asterisk) at low angles corresponding to (0*k*0) crystallographic planes of small-*n* perovskites, which indicates the enhancement of vertical orientation.[28] This would contribute to efficient charge transport toward the electron- and hole-accepting contacts along the inorganic metal halide octahedra layers, since the high energy barriers set by insulating organic cations are greatly suppressed,[35,39] as illustrated in Figure 4b. Moreover, the as-prepared perovskite films on PEDOT:PSS layer exhibit a lack of pinholes (see insets of Figure 4a) together with a significant decline in root-mean-square roughness (R_q) from 17.4 to 10.1 nm (Figure 4c,d), which demonstrates the vital effect of PEDOT:PSS layer in alleviating the inevitable surface roughness issue caused by ITO etching process, thus allowing high quality crystallization of perovskite films and better processing of subsequent layers for efficient charge transport with eliminated ionic migration as well as passivated carrier trapping and recombination.[40]

The introduction of PEDOT:PSS layer also leads to an overall increase in UV–vis absorption intensity, as revealed in Figure 4e, which accounts for spiking amounts of photogenerated carriers. Note that the absorption peak at around 520 nm becomes comparatively weaker, suggesting the reduction of $n = 1$ composition which is unfavorable for charge

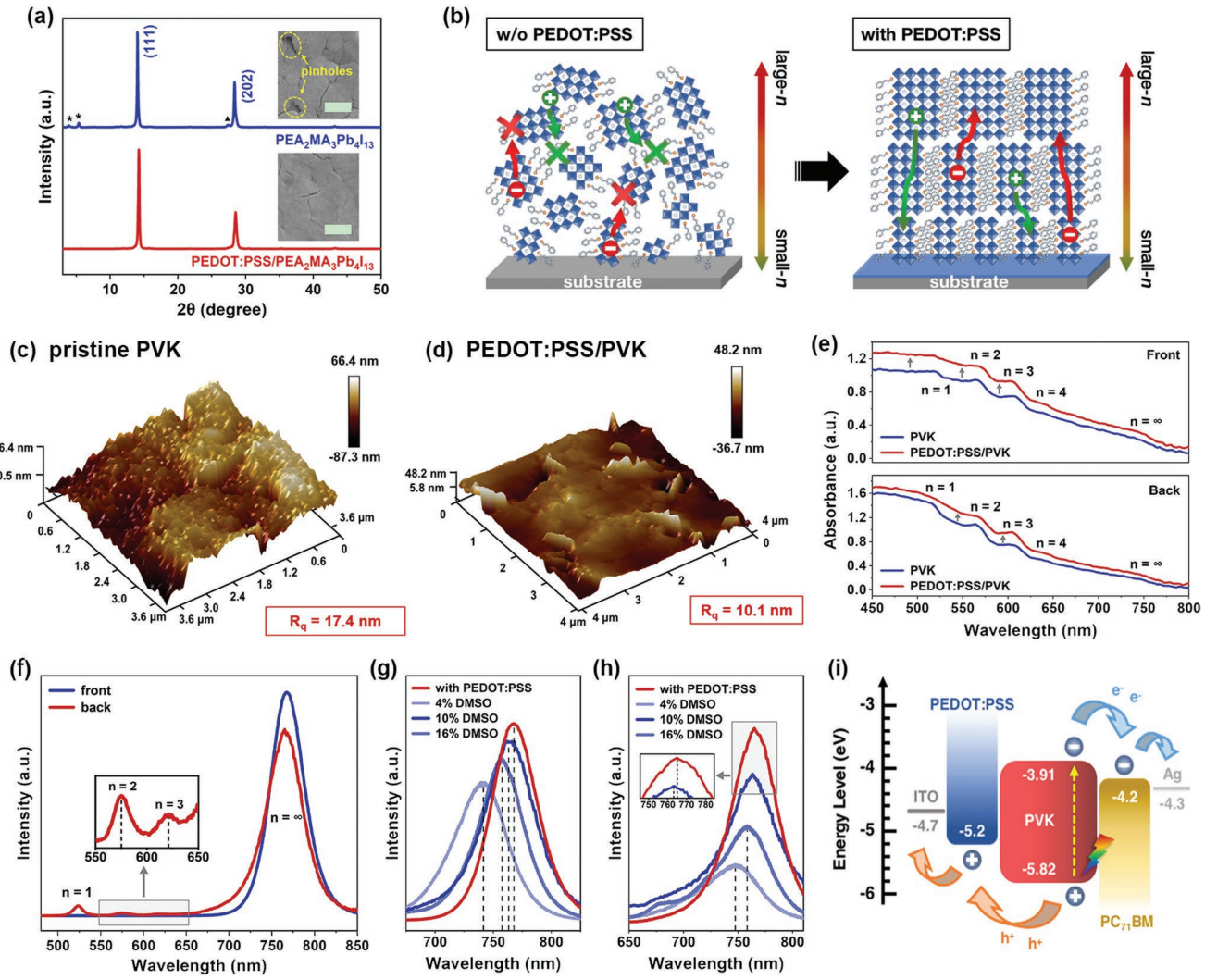

Figure 4. a) XRD patterns of pristine $PEA_2MA_3Pb_4I_{13}$ and PEDOT:PSS/$PEA_2MA_3Pb_4I_{13}$. The insets are corresponding top-view FESEM images (scale bar: 1 µm). b) Schematic illustration of the orientational growth of perovskite films without/with PEDOT:PSS layer and the corresponding out-of-plane charge transport. 3D AFM images of c) pristine $PEA_2MA_3Pb_4I_{13}$ and d) PEDOT:PSS/$PEA_2MA_3Pb_4I_{13}$. e) UV–vis absorption spectra of pristine $PEA_2MA_3Pb_4I_{13}$ and PEDOT:PSS/$PEA_2MA_3Pb_4I_{13}$, illuminated from the perovskite film side and the glass side. f) Steady-state PL spectra of PEDOT:PSS/$PEA_2MA_3Pb_4I_{13}$ illuminated from the perovskite film side and the glass side. The inset is the local enlarged curve. Local steady-state PL spectra corresponding to the dominant emission band, illuminated from g) the perovskite film side and h) the glass side. The inset is the local enlarged curve. i) Schematic illustration of band alignment in the ITO/PEDOT:PSS/PVK/$PC_{71}BM$/Ag photodetector.

transport. The steady-state PL spectra in Figure 4d show that the perovskite films grown on PEDOT:PSS layer still maintain good phase segregation characteristic along the vertical direction, which is consistent with that of UV–vis absorption spectra (Figure S6, Supporting Information). Meanwhile, the redshift of the dominant emission peak corresponding to $n = \infty$ composition manifest in the PL spectra tested from both sides of the sample (Figure 4e,f), which can be ascribed to the growth of crystallite size with the loss of quantum confinement, thus accelerating the charge transport.[41] The emission bands assigned to small-n phases present an obvious intensity loss in PL spectra after implementing the PEDOT:PSS layer (Figure 4f), compared with that of pristine $PEA_2MA_3Pb_4I_{13}$ (Figure 1c). This could be attributed to superior energy level match between PEDOT:PSS and perovskites, which encourages the efficient extraction of photogenerated holes from perovskites to the electrode layer while impeding carrier recombination,[42] as illustrated in Figure 4g. Here the valence band maxima (VBM) position of the perovskites is determined using ultraviolet photoelectron spectroscopy (UPS), and the conduction band minima is estimated by subtracting the VBM value from the optical bandgap (see Figure S7, Supporting Information). Time-resolved photoluminescence (TRPL) measurement was further carried out to evaluate the charge transport process. As shown in Figure S8 in the Supporting Information, the fitted average carrier lifetime (τ_{ave}) is well decreased from 523.51 to 94.54 ns after the introduction of PEDOT:PSS layer, which indicates the more efficient charge extraction at the PEDOT:PSS/PVK interface, thus corroborating the PL quenching result.

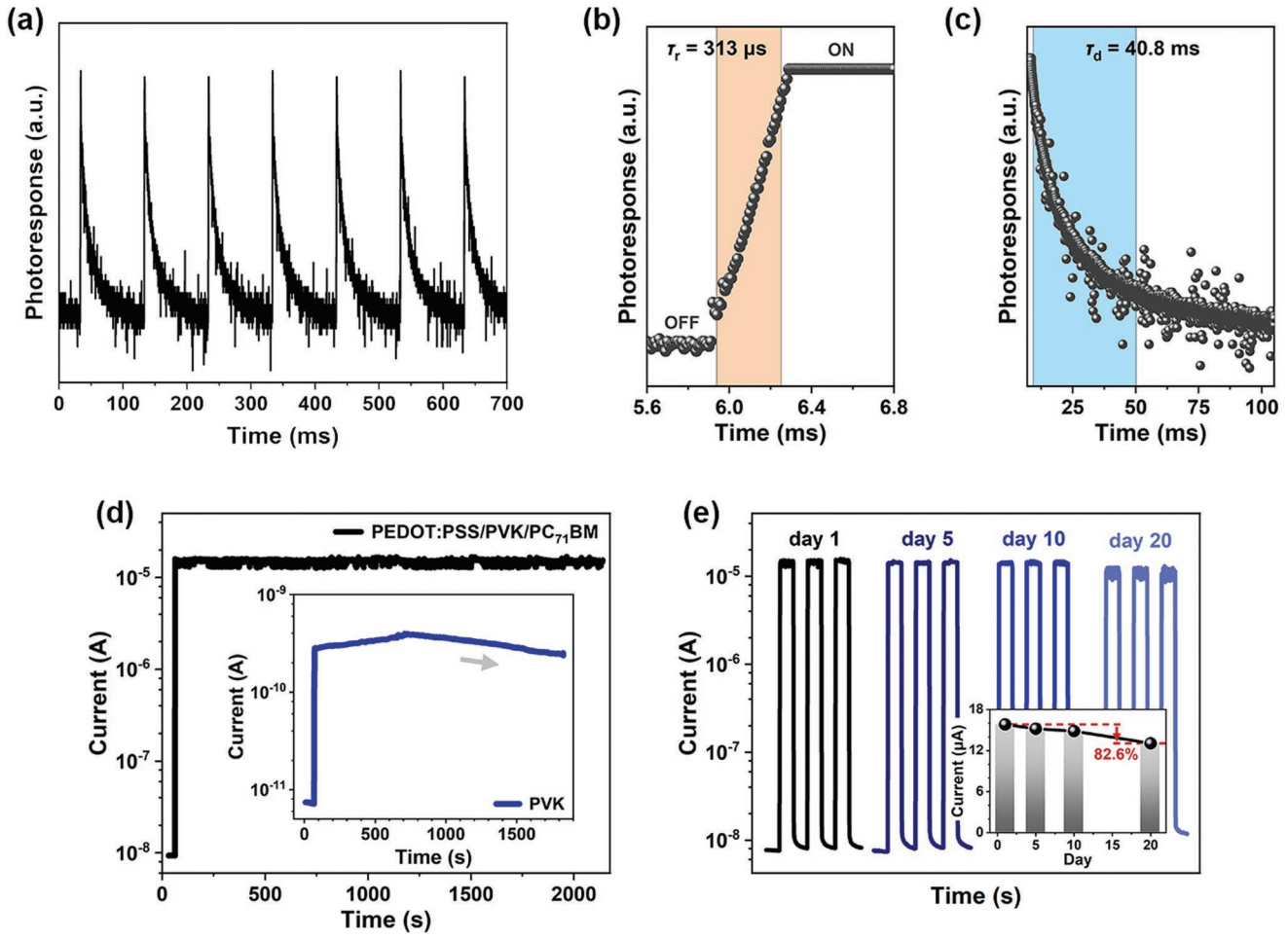

Figure 5. a) Photoresponse to 355 nm pulse laser with a modulation frequency of 10 Hz under 0 V bias. Estimated b) rise and c) decay time from single pulse response curve. d) The photocurrent curve of the ITO/PEDOT:PSS/PVK/$PC_{71}BM$/Ag device under continuous operation for 30 min at room temperature with the air humidity of 60%. The inset is that of ITO/PVK/Ag device. e) The semi-logarithmic *I–t* curves of the ITO/PEDOT:PSS/PVK/$PC_{71}BM$/Ag devices after 1, 5, 10, and 20 d of storage in air atmosphere. The inset is the corresponding photocurrent variation curve as the function of storage duration.

The transient photoresponse of the ITO/PEDOT:PSS/PVK/$PC_{71}BM$/Ag device is conducted under 355 nm pulse laser illumination without external bias voltage, as demonstrated in **Figure 5**a, where steady, rapid and repeatable photoresponse is observed with sharp pulse signal. Figure 5b,c display the time-resolved photoresponse of a single pulse, with the rise time (τ_r) and decay time (τ_d) estimated to be 313 μs and 40.8 ms, respectively. Furthermore, as depicted in Figure 5d, the photocurrent of ITO/PEDOT:PSS/PVK/$PC_{71}BM$/Ag device remains stable during the continuous operation for 30 min at room temperature with the air humidity of 60%, while the ITO/PVK/Ag device exhibits sharp degradation of photocurrent under the same condition, indicating the crucial role of $PC_{71}BM$ layer in protecting the perovskite films from direct contact with water and oxygen in the environment. After 20 d of storage in air atmosphere, the device still performs a fast and steady photoresponse with a slight attenuation of photocurrent to 82.6% of the initial value (Figure 5e), which proves the long-term stability and operating durability in air atmosphere.

3. Conclusion

In summary, quasi-2D RP perovskite films with uniform crystalline morphology and gradient phase distribution are successfully prepared via simple solvent engineering strategy, which gives rise to the enhancement of photoresponse under zero bias voltage. More specifically, the drastically improved self-powered optoelectronic performance originates mainly from the combined effect of the reduction of grain boundaries for rapid charge transport, together with proper gradient sedimentation resulting in cascaded type-II energy band arrangement perpendicular to the substrate, which brings about spontaneous separation of photogenerated carriers. Additionally, with the introduction of PEDOT:PSS layer, the upper perovskite films exhibit a preferable vertical orientation as well as a further decrease in surface roughness, which greatly avoid undesirable transport of charge carriers caused by disordered high energy barrier and poor crystalline quality, not to mention the spiking amounts of photogenerated carriers and optimized energy band matching inside the device.

The ITO/PEDOT:PSS/PVK/$PC_{71}BM$/Ag device therefore reaches a high on/off ratio of 2800, with the peak responsivity of 0.22 A W^{-1}, the detectivity up to 1.3×10^{12} Jones and the *EQE* over 80% at 330 nm. The device also displays a rapid and repeatable rise and decay time of 313 µs/40.8 ms, along with good tolerance to environmental conditions, demonstrating huge potential for long-term stable detection. It is believed that this work not only sheds light on the internal gradient distribution mechanism of perovskite compositions, but also sets the scene for future integration of high-performance photodetectors based on well-tuned quasi-2D perovskite thin films.

4. Experimental Section

Materials: PEAI (99.9%) and MAI (99.9%) were purchased from Advanced Election Technology Co. Ltd. Lead iodide (PbI_2, chemically pure, CP) and DMF (Analytical reagent, AR) were purchased from Sinopharm Chemical Reagent Co., Ltd. DMSO (99.7%) and $PC_{71}BM$ were purchased from J&K Chemicals Inc. PEDOT:PSS (CLEVIOS P VP AI 4083) was purchased from Heroes Inc. (Germany).

Device Fabrication: A series of precursor solutions were prepared by dissolving 0.2 mmol of PEAI, 0.3 mmol of MAI, and 0.4 mmol of PbI_2 in 1.0 mL of DMF/DMSO solvent mixture with varied DMSO contents, followed by magnetically stirring at 70 °C for 3 h and percolation. Before device fabrication, the ITO-patterned conductive glass substrates were ultrasonically cleaned in acetone, water, and ethanol for 20 min in turn, and then rendered hydrophilic through UV/ozone treatment for 5 min. Take the ITO/PVK/Ag device as an example, the cleaned substrate was first preheated on a hot plate at 130 °C for 15 min and transferred to a spin coater, followed by 75 µL of precursor solution spin-coated onto the hot substrate at 3000 rpm for 20 s. The perovskite layer was then annealed at 80 °C for 15 min. Patterned Ag films were finally prepared via vacuum thermal deposition as the top electrode. For ITO/PEDOT:PSS/PVK/$PC_{71}BM$/Ag device, the PEDOT:PSS solution was deposited onto the substrate at the spin rate of 3000 rpm for 40 s to form a thin film of 20 nm, while $PC_{71}BM$ layer was spin-coated after the sufficient cooldown of annealed device at 2000 rpm for 40 s.

Materials Characterization and Optoelectronic Measurement: The XPS pattern of the perovskite sample was obtained by using Thermo Scientific K-Alpha$^+$ under the excitation of mono Al Kα ($h\nu$ = 1486.6 eV). XRD patterns were carried out by Bruker D8 Advance X-ray diffractometer equipped with Cu K_α radiation (λ = 1.5406 Å). The morphology characterization was conducted by FESEM (Zeiss Sigma). The atomic force microscopy (AFM) images were acquired using Bruker Dimension Icon. The steady-state PL spectra and TRPL spectra were collected by Edinburgh FLS1000 spectrometer. The UV–vis absorption spectra were recorded with UV–vis spectrometer (Hitachi U-3900H). The UPS characterization was investigated by a monochromatic He I light source ($h\nu$ = 21.2 eV) and a vacuum generator (VG) Scienta R4000 analyzer. A sample bias of −5 V was applied to observe the secondary electron cutoff for precise work function calculation. The optoelectronic properties were measured with Keithley 4200-SCS and a 70 W xenon arc lamp equipped with a monochromator used as light source. The Nova II power meter (Ophir Photonics) was employed to detect the light intensity. The transient photoresponse was recorded using the 355 nm Q-switch Nd:YAG laser (Nd:$Y_3Al_5O_{12}$, Continuum Electro-Optics, MINILITE II) and the oscilloscope (Tektronix MSO/DPO5000).

Supporting Information

Supporting Information is available from the Wiley Online Library or from the author.

Acknowledgements

The authors thank Xinya Liu for the helpful discussions. This work was financially supported by National Key R&D Program of China (No. 2018YFA0703700), National Natural Science Foundation of China (Nos. 12061131009 and 51872050), and Science and Technology Commission of Shanghai Municipality (Nos. 21520712600 and 19520744300).

Conflict of Interest

The authors declare no conflict of interest.

Data Availability Statement

Data sharing is not applicable to this article as no new data were created or analyzed in this study.

Keywords

phase distribution, phase orientation, Ruddlesden-Popper perovskites, UV photodetectors

Received: October 14, 2022
Published online: January 1, 2023

[1] L. L. Mao, C. C. Stoumpos, M. G. Kanatzidis, *J. Am. Chem. Soc.* **2019**, *141*, 1171.
[2] J. Kang, J. H. Cho, *Phys. Chem. Chem. Phys.* **2020**, *22*, 13347.
[3] Z. Q. Li, E. L. Hong, X. Y. Zhang, M. Deng, X. S. Fang, *J. Phys. Chem. Lett.* **2022**, *13*, 1215.
[4] D. Thrithamarassery Gangadharan, D. L. Ma, *Energy Environ. Sci.* **2019**, *12*, 2860.
[5] X. He, M. Xia, H. Wu, X. Du, Z. Song, S. Zhao, X. Chen, G. Niu, J. Tang, *Adv. Funct. Mater.* **2022**, *32*, 2109458.
[6] S. Chen, G. Q. Shi, *Adv. Mater.* **2017**, *29*, 1605448.
[7] L. N. Quan, M. J. Yuan, R. Comin, O. Voznyy, E. M. Beauregard, S. Hoogland, A. Buin, A. R. Kirmani, K. Zhao, A. Amassian, D. H. Kim, E. H. Sargent, *J. Am. Chem. Soc.* **2016**, *138*, 2649.
[8] Y. N. Chen, Y. Sun, J. J. Peng, J. H. Tang, K. B. Zheng, Z. Q. Liang, *Adv. Mater.* **2018**, *30*, 1703487.
[9] S. G. Motti, T. Crothers, R. Yang, Y. Cao, R. Li, M. B. Johnston, J. P. Wang, L. M. Herz, *Nano Lett.* **2019**, *19*, 3953.
[10] J. W. Li, M. G. Wu, G. J. Yang, D. Y. Zhang, Z. J. Wang, D. Zheng, J. S. Yu, *Sol. Energy* **2020**, *205*, 44.
[11] I. C. Smith, E. T. Hoke, D. Solis-Ibarra, M. D. Mcgehee, H. I. Karunadasa, *Angew. Chem., Int. Ed.* **2014**, *53*, 11232.
[12] J. Hu, L. Yan, W. You, *Adv. Mater.* **2018**, *30*, 1802041.
[13] R. Shen, J. Y. Xu, X. Yao, Z. L. Guo, W. S. Yang, X. N. Ma, *J. Phys. Chem. Lett.* **2021**, *12*, 12336.
[14] J. C. Zhou, Y. L. Chu, J. Huang, *ACS Appl. Mater. Interfaces* **2016**, *8*, 25660.
[15] J. W. Lim, H. Wang, C. H. Choi, H. Kwon, L. N. Quan, W.-T. Park, Y.-Y. Noh, D. H. Kim, *Nano Energy* **2019**, *57*, 761.
[16] F. Mei, D. W. Sun, S. J. Mei, J. H. Feng, Y. M. Zhou, J. X. Xu, X. H. Xiao, *Adv. Phys.: X* **2019**, *4*, 1592709.
[17] H. Tsai, W. Nie, J. C. Blancon, C. C. Stoumpos, R. Asadpour, B. Harutyunyan, A. J. Neukirch, R. Verduzco, J. J. Crochet, S. Tretiak, L. Pedesseau, J. Even, M. A. Alam, G. Gupta, J. Lou, P. M. Ajayan, M. J. Bedzyk, M. G. Kanatzidis, A. D. Mohite, *Nature* **2016**, *536*, 312.

[18] Y. J. Yan, Y. G. Yang, M. L. Liang, M. Abdellah, T. Pullerits, K. B. Zheng, Z. Q. Liang, *Nat. Commun.* **2021**, *12*, 6603.
[19] F. Zhu, G. Lian, B. C. Yu, T. Zhang, L. Zhang, H. H. Yu, D. L. Cui, Q. L. Wang, H. J. Zhang, Q. B. Meng, C. P. Wong, *ACS Appl. Mater. Interfaces* **2022**, *14*, 1526.
[20] J. W. Kim, W. C. Lee, K. J. Cho, H. B. Ahn, J. H. Lee, K. Y. Baek, J. K. Kim, K. H. Kang, T. Lee, *Nanotechnology* **2021**, *32*, 185203.
[21] S. Sahayaraj, E. Radicchi, M. Ziółek, M. Ścigaj, M. Tamulewicz-Szwajkowska, J. Serafińczuk, F. De Angelis, K. Wojciechowski, *J. Mater. Chem. A* **2021**, *9*, 9175.
[22] L. Yan, J. Hu, Z. K. Guo, H. Chen, M. F. Toney, A. M. Moran, W. You, *ACS Appl. Mater. Interfaces* **2018**, *10*, 33187.
[23] H. L. Loi, J. P. Cao, X. Y. Guo, C. K. Liu, N. X. Wang, J. J. Song, G. Q. Tang, Y. Zhu, F. Yan, *Adv. Sci.* **2020**, *7*, 2000776.
[24] S. L. Wei, F. Wang, X. M. Zou, L. M. Wang, C. Liu, X. Q. Liu, W. D. Hu, Z. Y. Fan, J. C. Ho, L. Liao, *Adv. Mater.* **2020**, *32*, 1907527.
[25] Y. J. Chen, J. L. Hu, Z. H. Xu, Z. Y. Jiang, S. Chen, B. M. Xu, X. D. Xiao, X. H. Liu, K. Forberich, C. J. Brabec, Y. H. Mai, F. Guo, *Adv. Funct. Mater.* **2022**, *32*, 2112146.
[26] L. L. Min, W. Tian, F. R. Cao, J. Guo, L. Li, *Adv. Mater.* **2021**, *33*, 2101714.
[27] H. T. Lai, D. Lu, Z. Y. Xu, N. Zheng, Z. Q. Xie, Y. S. Liu, *Adv. Mater.* **2020**, *32*, 2001470.
[28] J. S. Shi, Y. R. Gao, X. Gao, Y. Zhang, J. J. Zhang, X. Jing, M. Shao, *Adv. Mater.* **2019**, *31*, 1901673.
[29] C. M. M. Soe, W. Nie, C. C. Stoumpos, H. Tsai, J. C. Blancon, F. Liu, J. Even, T. J. Marks, A. D. Mohite, M. G. Kanatzidis, *Adv. Energy Mater.* **2018**, *8*, 1700979.
[30] R. Quintero-Bermudez, A. Gold-Parker, A. H. Proppe, R. Munir, Z. Yang, S. O. Kelley, A. Amassian, M. F. Toney, E. H. Sargent, *Nat. Mater.* **2018**, *17*, 900.
[31] Z. Wang, Q. Wei, X. Liu, L. Liu, X. Tang, J. Guo, S. Ren, G. Xing, D. Zhao, Y. Zheng, *Adv. Funct. Mater.* **2021**, *31*, 2008404.
[32] T. F. Liu, Y. Y. Jiang, M. C. Qin, J. X. Liu, L. L. Sun, F. Qin, L. Hu, S. X. Xiong, X. S. Jiang, F. Y. Jiang, P. Peng, S. Y. Jin, X. H. Lu, Y. H. Zhou, *Nat. Commun.* **2019**, *10*, 878.
[33] M. J. Yuan, L. N. Quan, R. Comin, G. Walters, R. Sabatini, O. Voznyy, S. Hoogland, Y. B. Zhao, E. M. Beauregard, P. Kanjanaboos, Z. H. Lu, D. H. Kim, E. H. Sargent, *Nat. Nanotechnol.* **2016**, *11*, 872.
[34] Y. Qin, H. J. Zhong, J. J. Intemann, S. F. Leng, M. H. Cui, C. C. Qin, M. Xiong, F. Liu, A. K. Y. Jen, K. Yao, *Adv. Energy Mater.* **2020**, *10*, 1904050.
[35] Y. Yang, C. Liu, A. Mahata, M. Li, C. Roldán-Carmona, Y. Ding, Z. Arain, W. D. Xu, Y. H. Yang, P. A. Schouwink, A. Züttel, F. De Angelis, S. Dai, M. K. Nazeeruddin, *Energy Environ. Sci.* **2020**, *13*, 3093.
[36] F. Cao, L. Jin, Y. Wu, X. H. Ji, *J. Alloys Compd.* **2021**, *859*, 158383.
[37] Z. Q. Li, Z. L. Li, Z. F. Shi, X. S. Fang, *Adv. Funct. Mater.* **2020**, *30*, 2002634.
[38] Z. Q. Li, X. Y. Liu, C. L. Zuo, W. Yang, X. S. Fang, *Adv. Mater.* **2021**, *33*, 2103010.
[39] D. H. Cao, C. C. Stoumpos, O. K. Farha, J. T. Hupp, M. G. Kanatzidis, *J. Am. Chem. Soc.* **2015**, *137*, 7843.
[40] M. Xia, Z. Song, H. Wu, X. Du, X. He, J. Pang, H. Luo, L. Jin, G. Li, G. Niu, J. Tang, *Adv. Funct. Mater.* **2022**, *32*, 2110729.
[41] D. Baranov, S. Toso, M. Imran, L. Manna, *J. Phys. Chem. Lett.* **2019**, *10*, 655.
[42] Q. D. Yang, J. Li, Y. H. Cheng, H. W. Li, Z. Q. Guan, B. B. Yu, S. W. Tsang, *J. Mater. Chem. A* **2017**, *5*, 9852.